NANOSYSTEMS:
PHYSICS, CHEMISTRY, MATHEMATICS

Original article

Khamova T.V., Shilova O.A., et al. *Nanosystems: Phys. Chem. Math.*, 2022, **13** (4), 414–429.
http://nanojournal.ifmo.ru
DOI 10.17586/2220-8054-2022-13-4-414-429

Study of the structure and bioactivity of powdered iron oxides synthesized by sol-gel method

Tamara V. Khamova[1,a], Olga A. Shilova[1,b], Yulia E. Gorshkova[2,c], Natalia V. Tsvigun[3,d], Oleg V. Gerashchenko[4,e], Alexander E. Baranchikov[5,f], Olga R. Udalova[6,g], Anna S. Zhuravleva[6,h], Gaiane G. Panova[6,i], Gennady P. Kopitsa[1,4,k]

[1]Institute of Silicate Chemistry of Russian Academy of Sciences, St. Petersburg, Russia

[2]Joint Institute for Nuclear Research, Dubna, Moscow Region, Russia

[3]Institute of Crystallography Federal R&D Center "Crystallography and Photonics" of the Russian Academy of Sciences, Moscow, Russia

[4]Petersburg Nuclear Physics Institute named by B. P. Konstantinov of National Research Centre Kurchatov Institute, Gatchina, Leningrad Region, Russia

[5]Kurnakov Institute of General and Inorganic Chemistry of the Russian Academy of Sciences, Moscow, Russia

[6]Agrophysical Research Institute, St. Petersburg, Russia

[a]tamarakhamova@gmail.com, [b]olgashilova@bk.ru, [c]Yulia.Gorshkova@jinr.ru, [d]n_tsvigun@mail.ru, [e]gerashchenko_ov@pnpi.nrcki.ru, [f]a.baranchikov@yandex.ru, [g]udal59@inbox.ru, [h]zhuravlan@gmail.com, [i]gaiane@inbox.ru, [k]kopitsa_gp@pnpi.nrcki.ru

Corresponding author: Tamara V. Khamova, tamarakhamova@gmail.com

PACS 61.10.Eq, 61.12.Ex

ABSTRACT Magnetite (Fe_3O_4) and maghemite with an admixture of hematite (γ-Fe_2O_3/α-Fe_2O_3) powders are synthesized via sol-gel process and characterized using XRD, SEM, low temperature nitrogen adsorption, small-angle X-ray scattering (SAXS) and small-angle polarized neutron scattering (SAPNS). The synthesized γ-Fe_2O_3/α-Fe_2O_3 and Fe_3O_4 samples are found to be porous systems featuring with a three-level hierarchically organized structure with different intrinsic scales and aggregation types for each of the structural levels. For both materials, the intrinsic size of the highest level exceeds 70 nm, and magnetic structure involves superparamagnetic particles with a characteristic radius of magnetic-nuclear cross-correlations $R_{MN} \approx 3$ nm. The biological activity of γ-Fe_2O_3/α-Fe_2O_3 and Fe_3O_4 aqueous suspensions in certain concentrations in respect to seed treatment, growth and productivity of plants was studied using the example of spring barley variety Leningradsky under adjustable favorable conditions and physical modeling of stress effects (irradiation with high-intensity UV-B radiation, soil moisture deficiency).

KEYWORDS sol-gel synthesis, iron oxides, mesostructure, magnetic structure, seed presowing treatment

ACKNOWLEDGEMENTS The XRD measurements were performed using the equipment of the Shared Research Center FSRC "Crystallography and Photonics" RAS and were supported by the Russian Ministry of Education and Science. The SEM measurements were performed using shared experimental facilities supported by IGIC RAS state assignment. SAPNS measurements were performed using the equipment of the Jülich Centre for Neutron Science, Forschungszentrum Jülich GmbH, Outstation at MLZ, Garching, Germany. This work was supported by the Ministry of Science and Higher Education of the Russian Federation as part of the IChS RAS state assignment (project 0081-2022-0006) and as part of the Agrophysical Research Institute state assignment No. FGEG-2022-0005.

FOR CITATION Khamova T.V., Shilova O.A., Gorshkova Yu.E., Tsvigun N.V., Gerashchenko O.V., Baranchikov A.E., Udalova O.R., Zhuravleva A.S., Panova G.G., Kopitsa G.P. Study of the structure and bioactivity of powdered iron oxides synthesized by sol-gel method. *Nanosystems: Phys. Chem. Math.*, 2022, **13** (4), 414–429.

1. Introduction

Magnetic nanoparticles of iron oxides attract a permanent interest of researchers due to a wide range of applications in various fields, including magnetic resonance imaging, memory devices, sensors, spintronics, magnetic targeted drug delivery, biomedicine, and environment decontamination [1–5]. Recently, iron oxide nanoparticles have become of particular interest for crop production due to a positive effect on the growth, development, and productivity of agricultural

plants [6–15]. However, this effect can be ambiguous depending on a certain type of plant cultures, crystalline modification of iron oxides, their particle size and concentration in the preparation used to treat plants, as well as the type of plant culture. Therefore, a thorough study of the influence of iron oxides composition, structure, size and concentration on the development of various plant cultures is an essential practically important goal.

Various synthesis methods are used to obtain iron oxide powders: chemical precipitation, mechanochemical method, emulsion method, hydrothermal method, and sol-gel method [16–23]. Each of the above methods has its own advantages and disadvantages. The advantages of the sol-gel method include the simplicity and low cost of the technological process, the high chemical homogeneity of the materials obtained, low temperature of the synthesis and possibility for the adjustment of the target properties of the resulting materials.

The structure of nanosized magnetic powders, including iron oxides, is commonly characterized using XRD, SEM, TEM low-temperature nitrogen adsorption techniques. However, these methods provide the information only about the structural organization on the atomic level. Magnetic properties of such systems are usually studied by such methods as measuring magnetization of samples depending on the applied magnetic field. Such techniques do not allow any data about the structure and characteristic dimensions of the magnetic phases in the studied materials. These parameters can be determined using small-angle polarized neutron scattering (SAPNS) [24,25] affording measurements of magnetic-nuclear interference scattering [26–29].

In our earlier studies, a positive effect of presowing seed treatment, as well as foliar treatment of plants with suspensions of iron oxide nanoparticles synthesized by chemical precipitation, on the germination of seeds, morphometric indicators of growth and their biochemical performances of plants was revealed [30]. This paper repots the continuation of this research in respect to study of the composition and structure of iron oxide powders synthesized by the sol-gel method and effect of their use on the efficiency of pre-sowing seed treatment of spring barley (Leningradsky variety) at the early stages of its development and eventually upon the productivity when growing plants under controlled favorable and stressful conditions.

2. Synthesis and characterization techniques

Magnetite and maghemite were prepared and characterized in this study. Magnetite nanoparticles were synthesized via sol-gel procedure using iron nitrate ($Fe(NO_3)_3 \cdot 9H_2O$) and ethylene glycol ($C_2H_4(OH)_2$), with drying the prepared gel in vacuum. To prepare the sol, 0.1 mol iron nitrate was dissolved in 50 mL ethylene glycol followed by mixing thus obtained solution using a magnetic stirrer at 40 °C within 2 hours. Then the obtained sol was then kept at 80 °C in an oven for approximately 30 min until a brown gel was formed. The resulting gel was aged and then dried at 120 °C for 4 hours. After drying, the xerogel was subjected to vacuum heat treatment at 300 °C for 2 hours. As a result, a consolidated product was obtained and subsequently crumbled into a black powder upon mechanical impact. To prepare maghemite nanoparticles, the resulting black powder was heated in air in an oven at 300 °C for 2 hours. As a result, a red-brown powder was obtained. The synthesis of magnetite nanoparticles was performed according to a similar procedure. The prepared black powder was heated in air in an oven at 300 °C for 2 hours to yield a red-brown target powdered product.

The structure of the prepared iron oxide powders was studied using the following techniques. The phase composition and crystal structure of the powders were characterized by powder X-ray diffraction (XRD) using a Rigaku Miniflex 600 diffractometer. The lattice parameters were calculated by the least squares method using the PDWin software package. The microstructure of the samples was analyzed using a Carl Zeiss NVision 40 high resolution scanning electron microscope (SEM) with an Oxford Instruments X-MAX detector (80 mm^2) at the accelerating voltage of 1 kV.

The texture characteristics of the powders were analyzed by low-temperature nitrogen adsorption using a Quantachrome Nova 1200e analyzer. Before measurements, the samples were degassed at 100 °C in vacuum for 15 – 16 h. The specific surface area of the samples (S_{sp}) was determined using the Brunauer–Emmett–Teller model by 7 points in the range of nitrogen partial pressures $P/P_0 = 0.07 \div 0.25$. The specific pore volume was measured at nitrogen partial pressure $P/P_0 = 0.995$. The pore size distribution was calculated by analyzing the desorption branches of full adsorption-desorption isotherms (in the range of nitrogen partial pressures $0.01 \ldots 0.99$) using the Barrett–Joyner–Halenda (BDH) model.

The structure of iron oxide powders was studied at the mesoscopic scale by SAXS method. SAXS measurements were carried out using the Xeuss 3.0 SAXS/WAXS System (Joint Institute for Nuclear Research, Dubna, Russia) operating in point geometry, and using a GeniX3D microfocus generator of X-ray radiation with Mo$K\alpha$ ($\lambda = 0.071069$ nm), operating in the 30 W/30 μm mode. The spectrometer was equipped with a moving detector Eiger2 R 1M with a sensitive area of 77.1×79.7 mm^2 (pixel size 75 μm). The measurements using two distances from the sample to detector (400 and 4500 mm) enabled the determination of the of X-ray scattering intensity $I(q)$ in the range of momentum transfer of $0.05 < q < 6$ nm^{-1} ($q = (4\pi/\lambda)\sin(\theta/2)$, where λ is the incident X-ray wavelength and θ is the scattering angle).

For the studied iron oxide powders, the measurements were carried out in vacuum at room temperature. To obtain the differential small angle scattering cross section $d\Sigma(q)/d\Omega$ in absolute units, we used a conventional procedure for normalization of the scattering cross section of amorphous carbon (Glassy Carbon), which gives a plateau with an intensity of 3.805 cm^{-1} upon scattering at small angles in the region of $0.1 < q < 0.9$ nm^{-1}. This value is almost 250 times greater than the corresponding value for water H_2O, thus offering a more accurate value of the intensity in absolute terms.

The magnetization of iron oxide powders was measured using the induction method. An ampoule wound round with a measuring inductance coil was placed in a uniform sinusoidal alternating magnetic field with a frequency of 50 Hz generated by a Helmholtz coil. The induced voltage measurements were carried out for the ampoule without a sample and with the sample placed in the ampoule. The specific magnetization was calculated from the difference between these data.

The magnetic structure of iron oxide powders was studied using a small-angle polarized neutron scattering (SAPNS), including the measurement of magnetic-nuclear interference. SAPNS measurements were carried out using a small-angle diffractometer KWS-1 (FRM-II reactor, Garching, Germany) operating in a mode close to point geometry. The measurements were performed using a beam of polarized neutrons with the initial polarization $P_0 \cong 0.95$ and wavelength $\lambda = 0.5$ nm with $\Delta\lambda/\lambda = 0.1$. The sample-detector distance SD = 8 m made it possible to measure the intensity of neutron scattering in the range of transmitted pulses $0.08 < q < 1$ nm^{-1}. The scattered neutrons were recorded by a two-dimensional scintillation position-sensitive detector based on ^{6}Li (128×128 cells with a spatial resolution of 5×5 mm^2).

The studied iron oxide powders were placed in a 1 mm thick quartz cell. The measurements were carried out in a "zero" field H close to zero value, and an external magnetic field $\boldsymbol{H} = 1T$ applied in the horizontal direction rectangular to the incident neutron beam. In the experiment, the dependence of the intensity of scattered neutrons upon the transferred momentum q was measured for neutron polarization P_0 directed parallel $I^+(q, P_0^+)$ and antiparallel $I^-(q, P_0^-)$ to the external magnetic field. The initial spectra were corrected using the standard procedure [31], taking into account the scattering by the installation armature and quartz cell, as well as the laboratory hall background.

To separate the isotropic and anisotropic scattering components, the intensity was radially averaged in the vicinity of the angles $\alpha = 0$ and $\pi/2$ in the detector plane (with the averaging sector $\pm 2\ ^\circ$), corresponding to the directions along and across the applied magnetic field $\boldsymbol{H}$. This averaging results were inserted in the following system of equations:

$$I^+(q,0) = I^+_{\parallel}(q) = \left\langle F_N^2 \right\rangle, \tag{1a}$$

$$I^+(q,\frac{\pi}{2}) = I^+_{\perp}(q) = \left\langle F_N^2(q) \right\rangle + \left\langle F_M^2(q) \right\rangle - 2P \left\langle F_N(q) F_M(q) \right\rangle, \tag{1b}$$

$$I^-(q,0) = I^-_{\parallel}(q) = \left\langle F_N^2 \right\rangle, \tag{1c}$$

$$I^-(q,\frac{\pi}{2}) = I^-_{\perp}(q) = \left\langle F_N^2(q) \right\rangle + \left\langle F_M^2(q) \right\rangle + 2P\varepsilon \left\langle F_N(q) F_M(q) \right\rangle. \tag{1d}$$

Based on the experimental data, this system was resolved to determine the nuclear $\left\langle F_N^2(q) \right\rangle$, magnetic $\left\langle F_M^2(q) \right\rangle$ and interference $\langle F_N(q) F_M(q) \rangle$ contributions to the overall scattering intensity $I(q) = (I^+(q, P_0^+) + I^-(q, P_0^-))/2$.

Assuming that nuclear scattering is independent on the external magnetic field $\boldsymbol{H}$, the magnetic contribution to the scattering intensity in the case of "zero" field was determined as:

$$\left\langle F_M^2(q) \right\rangle_{\boldsymbol{H}\approx 0} = \frac{3}{2} \cdot (I_{\boldsymbol{H}\approx 0}(q) - \left\langle F_N^2 \right\rangle_{\boldsymbol{H}=1T}). \tag{2}$$

To derive the absolute values, the obtained scattering intensities were normalized to the incoherent scattering cross section of plexiglass, taking into account the detector efficiency [31] and bulk density ρ_b for each of the samples. The preliminary processing of the obtained data was carried out using QtiKWS software program [32].

The study of the iron oxide powders biological activity involved the determination of the effect of their treatment with aqueous suspensions of a test plant crop seeds upon the germination energy, seed germination and biometric indicators of seedling growth, as well as on the plant productivity when they are grown in intensive artificial light culture under favorable controlled and under the stress factors action (soil moisture deficiency, high-intensity UV-B radiation). The object of the study was spring barley of the Leningradsky variety from the collection of the N. I. Vavilov All-Russian Institute of Plant Genetic Resources (VIR). The seed treatment was carried out with aqueous suspensions of iron oxide powders at concentrations of 0.01 and 0.001 mg per 1 liter of water according to the procedure [30]. The seeds treated with distilled water were used as reference samples. Germination of seeds and determination of their germination energy were carried out according to the Russian Standard GOST 12038–84. On the 3rd day after soaking, the energy of seed germination was assessed, on the 7th day – their germination, and the length of the sprouts and roots was also measured. Each variant of the experiment was performed for 400 seeds. The studies were carried out in accordance with the rules of the International Seed Testing Association (ISTA).

To study the effect of presowing seed treatment on the production process, the seeds were sown in 3 L plastic vessels filled with 3 kg of soddy-podzolic sandy loamy soil (A arable layer) fertilized at the rate of kg of active substance per 1 ha – N90P90K90. The plants were grown in special plants growing light equipment with a usable area of 1.5 m^2 developed at the Agrophysical Research Institute [33]. The equipment are equipped with lifting light blocks involving DNaZ-400 lamps as light sources. The duration of the light period was 14 hours, the irradiance of plants was 85 – 90 W/m^2 in the photosynthetically active radiation range; the temperature was maintained within the limits of $+22 \ldots 24\ ^\circ$C during the day and $+18 \cdots + 20\ ^\circ$C at night, the relative air humidity was 65 ± 5 %. The oxidative stress conditions in plants in the tubing phase of their development was achieved by a single irradiation with high-intensity UV-B radiation at a dose of

20.0 kJ/m^2; LE-30 lamps (Russia) with a spectral range of 280 – 380 nm and an intensity maximum at $\lambda = 320$ nm were used as the source of UV-B radiation. Physical modeling of soil moisture deficiency was performed during the period of development (tillering – budding) by maintaining soil moisture in some vessels at a level of 25 – 30 % of the total moisture capacity for 21 days, after which the level of soil moisture in these options was increased to the level in the reference samples (60 – 65 % of the total moisture capacity). The plants grown from seeds treated with distilled water on soil with a favorable moisture level of 60 – 65 % of the total moisture capacity and unexposed to UV-B radiation were used as control samples. The stage of plants development at the time of harvesting was full maturation. Every variant of the experiment involved 24 plants, number of vegetation experiments – 2.

3. Results and discussion

3.1. Characterization of the composition and structure of the synthesized powders

XRD profiles of the synthesized iron oxide powders (Fig. 1) demonstrate broad diffraction peaks suggesting that the synthesized samples are poorly crystallized. This conclusion is further confirmed by SEM data (Fig. 2) indicating a porous poorly crystallized aggregated structure of the studied materials.

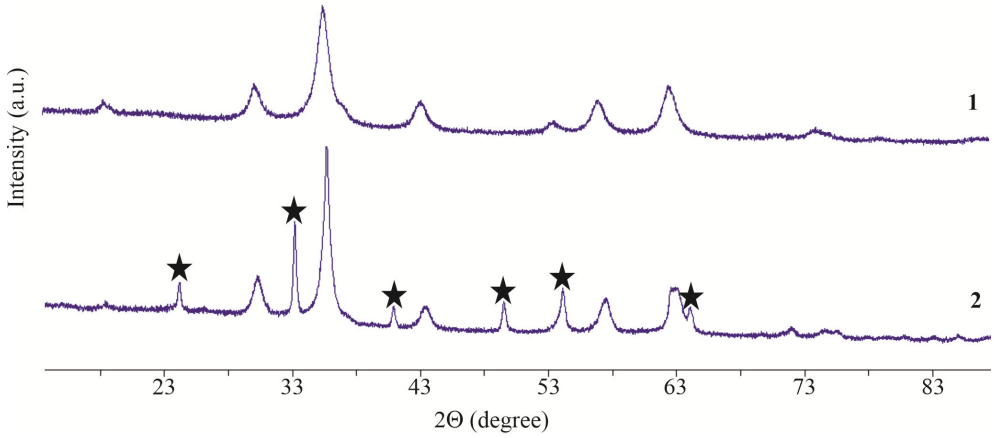

FIG. 1. XRD profiles of the synthesized iron oxide powders: 1 – Fe_3O_4; 2 – γ-Fe_2O_3/α-Fe_2O_3 (asterisks correspond to hematite phase)

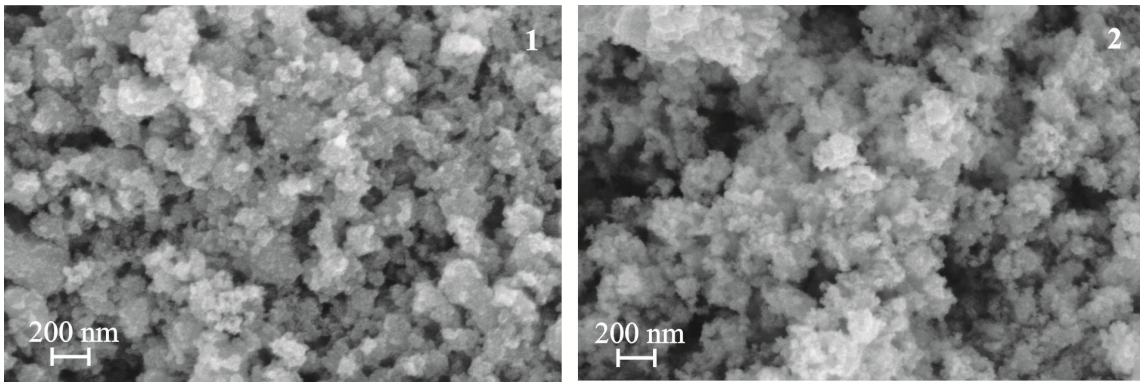

FIG. 2. SEM images of the synthesized iron oxide powders: 1 – Fe_3O_4; 2 – γ-Fe_2O_3/α-Fe_2O_3

Since magnetite and maghemite have almost the same crystal lattice structure with almost coinciding positions of diffraction peaks, in order to distinguish between them, the unit cell parameters were calculated (Table 1).

According to Table 1, the cell parameters of the black iron oxide powder are close to the reference values for magnetite (Fe_3O_4), while the cell parameters of the red-brown powder are closer to those for maghemite (γ-Fe_2O_3). In addition, peaks relating to the hematite phase (α-Fe_2O_3) are observed in the diffraction pattern of the red-brown powder. Thus, the data obtained suggest that the powders synthesized by sol-gel method are iron oxide in the forms of magnetite (Fe_3O_4) and maghemite with an admixture of hematite (γ-Fe_2O_3/α-Fe_2O_3).

The full nitrogen adsorption-desorption isotherms for the synthesized iron oxide powders are shown inn Fig. 3(a,c). The presence of capillary-condensation hysteresis makes it possible to attribute these isotherms to type IV according to the IUPAC classification, which is typical for mesoporous materials containing pores with a diameter of 2 – 50 nm. As

TABLE 1. Unit cell parameters and D_{CSR} estimation for the synthesized iron oxide powders in comparison with reference data

Synthesized samples	Powder color	D_{CSR}, nm	Unit cell parameters, Å	
			Reference	Calculated
Fe_3O_4	Black	8	8.396 – 8.397	8.402(3)
γ-Fe_2O_3/α-Fe_2O_3	Red-brown	11.6	8.336 – 8.339	8.352(4)

can be seen from these figures, the shape of the hysteresis loops for the synthesized samples is close to the H2 type, suggesting the presence of bottle-shaped mesopores in them. In addition, the closing of hysteresis loops for both samples at values of relative pressure P/P_0 less than 0.3 (Fig. 3(a)) indicates the presence of a significant amount of micropores. The results of the obtained isotherms analysis using BET and BDH models are presented in Fig. 3(b,d) and Table 2.

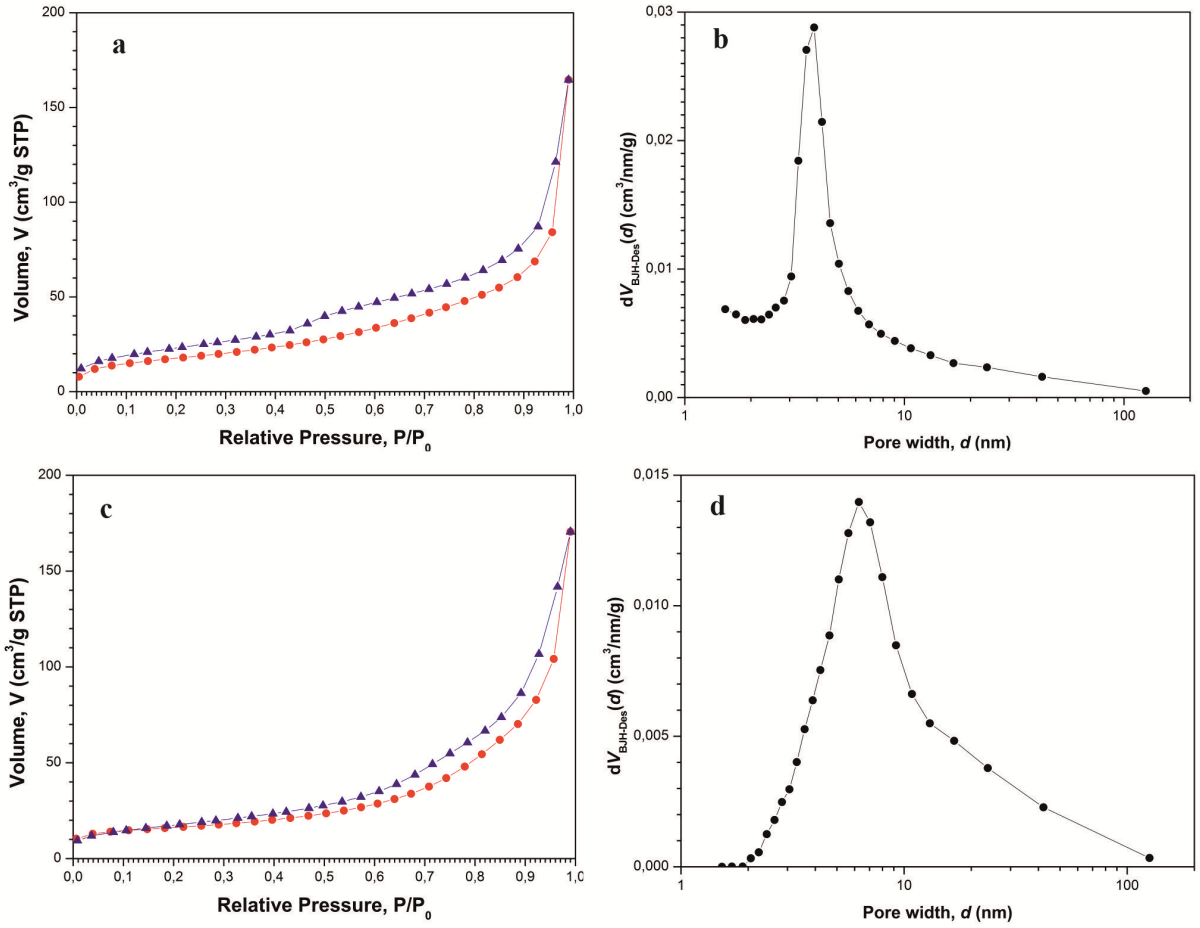

FIG. 3. Full nitrogen adsorption-desorption isotherms (a, c) and pore size distributions (b, d) based on the isotherms processing using the Barrett–Joyner–Halenda (BDH) model for the synthesized Fe_3O_4 (a, c) and γ-Fe_2O_3/α-Fe_2O_3 (b, d)

As shown in Table 2, the synthesized Fe_3O_4 and γ-Fe_2O_3/α-Fe_2O_3 powders have a well-developed surface, similar values of the specific surface area ($S_{BET} \approx 64$ and 58 m^2/g, respectively) and the same quite large specific pore volume ($V_{P/P_0 \to 0.99} = 0.26$ cm^3/g). In addition, for the synthesized Fe_3O_4, a normal (almost symmetrical) pore size distribution is observed with the maximum at $d_p \approx 4$ nm, while γ-Fe_2O_3/α-Fe_2O_3 features with a lognormal distribution of pore $dV(D)$ with the maximum at $d_p \approx 6$ nm.

To obtain more complete information about the supramolecular structure organization of the (size and shape of inhomogeneities, type of their aggregation) in the studied iron oxide powders, SAXS method affording the mesostructure characterization for various materials in the scale range from 1 to 100 nm. A double logarithmic scale plot for the experimental data on the differential macroscopic cross section $d\Sigma(q)/d\Omega$ of small-angle X-ray scattering versus the transferred

TABLE 2. Textural parameters (specific surface area S_{BET}; specific pore volume V_{sp}; average pore diameter, d_p) of the synthesized iron oxide powders determined from the analysis of full nitrogen adsorption-desorption isotherms using BET and BDH models

Powdered iron oxides	S_{BET}, m^2/g	$V_{P/P_0 \cong 0.995}$, cm^3/g	d_p, nm BDH (des.)
Fe_3O_4	63.5 ± 1.2	0.26	3.9
γ-Fe_2O_3/α-Fe_2O_3	57.5 ± 0.6	0.26	6.3

momentum q for the studied Fe_3O_4 and γ-Fe_2O_3/α-Fe_2O_3 powders is shown in Fig. 4. These data clearly indicate that the scattering on γ-Fe_2O_3/α-Fe_2O_3 sample is significantly higher compared with Fe_3O_4 in the entire range of q values, suggesting its lower nuclear density homogeneity on the mesoscopic scale (1... 100 nm).

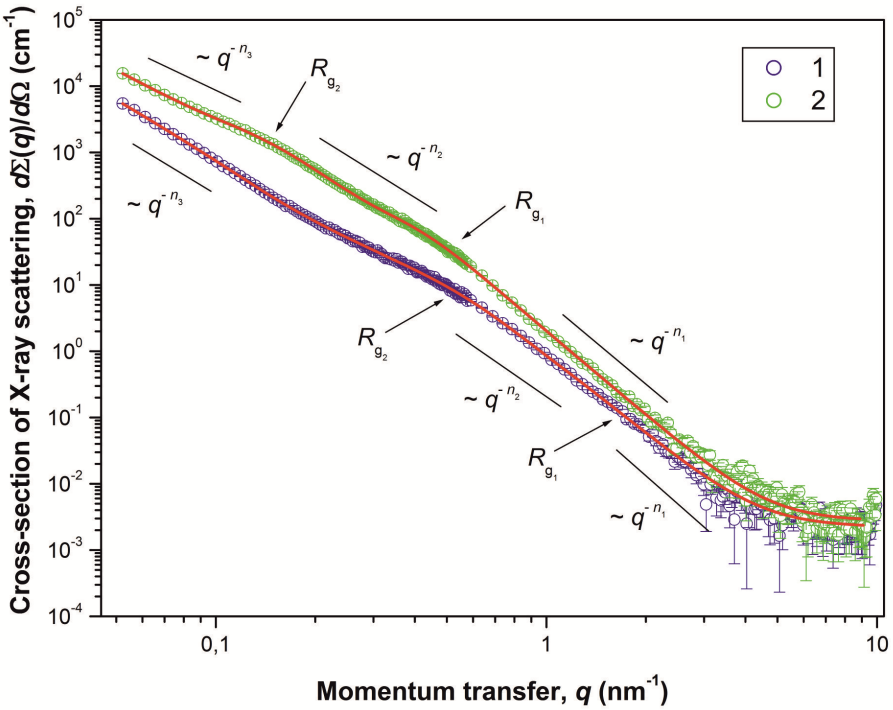

FIG. 4. Differential SAXS cross-section $d\Sigma(q)/d\Omega$ from iron oxide samples Fe_3O_4 (1) and γ-Fe_2O_3/α-Fe_2O_3 (2). Solid lines correspond to the experimental data fits according to the equation (4)

A common feature for both samples under study is the presence on the corresponding scattering curves of three ranges in terms of the transferred momentum q, where the behavior of the scattering cross section $d\Sigma(q)/d\Omega$ follows the power laws $q^{-\Delta}$ with different values $\Delta = n_1$, n_2 and n_3, respectively. In the intermediate regions, near the crossover points q_c (transition points between different scattering modes), the SAXS scattering cross section $d\Sigma(q)/d\Omega$ is satisfactorily described by an exponential dependence (Guinier mode). Thus, the scattering pattern observed for the synthesized iron oxide powders is typical of scattering on three-level hierarchical porous structures [34–36], with different characteristic scales and aggregation types for each of the levels. Moreover, the convex shape of the $d\Sigma(q)/d\Omega$ ($n_1 > n_2 > n_3$) curves clearly indicates that the inhomogeneities of the subsequent structural level with larger in characteristic size R_c are formed from smaller inhomogeneities of the previous structural level, i.e. $R_{c3} > R_{c2} > R_{c1}$. The estimates of the characteristic size R_c for inhomogeneities at each structural level, corresponding to the upper limit of self-similarity for fractal systems, can be obtained from the analysis of scattering in the Guinier mode near the crossover points q_c from the relations $R_c = \sqrt{(5/3)} \cdot R_g$ (in the case of spherical particles with an almost smooth surface [37]) and $R_c = [(D+2)/D]^{1/2} \cdot R_g$ (in the case of fractal objects [38]), where R_g is the gyration radius of the scattering inhomogeneity and D is the fractal dimension. It should be noted that the R_c estimate obtained from the analysis in the Guinier mode corresponds to the maximum size of the scattering inhomogeneities of this type, i.e. always corresponds to the upper estimate.

Scattering from the first (smaller scale) of these structural levels, observed for Fe_3O_4 at $q > 1.5$ nm^{-1} and at $q > 0.5$ nm^{-1} for γ-Fe_2O_3/α-Fe_2O_3 is described by the power dependence q^{-n1}. The power factor n_1 determined from the slope of linear parts in the experimental plots curves $d\Sigma(q)/d\Omega$ in a double logarithmic scale are 4.02 ± 0.04 for

Fe_3O_4 and 4.04 ± 0.04 for γ-Fe_2O_3/α-Fe_2O_3, respectively. This means that both samples feature with scattering by inhomogeneities with almost smooth boundaries $D_{S1} = 2.02 \pm 0.04$ and 2.04 ± 0.04 ($n = 4$ according to the Porod law [39]) in the X-ray wavelength range of the used in this experiment ($\lambda_{\mathrm{MoK}\alpha} = 0.071$ nm).

Scattering from the second structural level, observed for the Fe_3O_4 and γ-Fe_2O_3/α-Fe_2O_3 samples in the ranges $0.5 < q < 1.4$ nm^{-1} and $0.15 < q < 0.4$ nm^{-1} is described by the power dependence q^{-n2} with the power factor $n_2 = 3.42 \pm 0.04$ and 2.69 ± 0.04, respectively. Thus, in the case of Fe_3O_4, scattering takes place at inhomogeneities (clusters) with a highly developed fractal phase interface (solid phase – pore) [40] with the dimension defined as $D_{S2} = 6 - n_2 = 2.58 \pm 0.02$, while for oxide γ-Fe_2O_3/α-Fe_2O_3 the power factor $1 < n_2 < 3$ corresponds to scattering by objects (clusters) with mass-fractal aggregation of inhomogeneities [41] with the fractal dimension $D_{M2} = n_2 = 2.69 \pm 0.04$.

The lower limit of self-resemblance for surface-fractal (Fe_3O_4) and mass-fractal (γ-Fe_2O_3/α-Fe_2O_3) clusters of a given structural level is determined by the characteristic size R_{c1} of inhomogeneities of the 1st structural level. An estimate of the upper limit of self-resemblance R_{c2} for fractal clusters of the 2nd structural level, in both cases, was obtained from the analysis of scattering in the Guinier mode in the ranges $0.3 < q < 0.5$ nm^{-1} for Fe_3O_4 sample and $0.1 < q < 0.15$ nm^{-1} for γ-Fe_2O_3/α-Fe_2O_3 (see Table 3).

TABLE 3. Mesostructure parameters of the synthesized iron oxide powders obtained from SAXS data analysis

Parameters	Synthesized iron oxides	
	γ-Fe_2O_3/α-Fe_2O_3	Fe_3O_4
3rd structural level		
R_{c3}, nm	> 70	
B_3, cm^{-1}nm^{-n3}	18 ± 4	0.56 ± 0.05
$D_{M3} = n_3$	2.25 ± 0.02	—
$D_{S3} = 6 - n_3$	—	2.87 ± 0.02
2nd structural level		
G_2, cm^{2}g^{-1}	2700 ± 500	31 ± 2
$R_{c2} = [(D_{S2,M2} + 2)/D_{S2,M2}]^{1/2} \cdot R_{g2}$, nm	18.0 ± 2	5.5 ± 0.5
B_2, cm^{-1}nm^{-n2}	7.2 ± 1.1	1.1 ± 0.3
$D_{M2} = n_2$	2.69 ± 0.04	—
$D_{S2} = 6 - n_2$	—	2.58 ± 0.04
$Z = [(R_{g2})^2/(R_{g1})^2]^{D/2}$	24	15
1st structural level		
G_1, cm^{-1}	95 ± 22	1.8 ± 0.2
$R_{c1} = \sqrt{(5/3)} \cdot R_{g1}$, nm	5.4 ± 0.6	1.9 ± 0.2
B_1, cm^{-1}nm^{-n1}	1.9 ± 0.06	0.88 ± 0.08
n_1	4.04 ± 0.04	4.02 ± 0.04
$I_{inc} \cdot 10^3$, cm^{-1}	2.5 ± 0.2	2.3 ± 0.2

Note: G_1 and G_2 are Guinier prefactors for the 1st and 2nd structural levels; B_1, B_2 and B_3 are power prefactors for the 1st, 2nd and 3rd structural levels; R_{c1} and R_{c2} are characteristic sizes of inhomogeneities at the 1st and 2nd structural levels; D_{S2} (D_{M2}) and D_{S3} (D_{M3}) are fractal dimensions of surface-fractal (mass-fractal) clusters of the 2nd structural level and aggregates of the 3rd structural level, Z is the degree of primary particles aggregation in a fractal cluster.

Scattering from the third (the largest size) structural level, observed for the Fe_3O_4 and γ-Fe_2O_3/α-Fe_2O_3 samples in the ranges $q < 0.3$ nm^{-1} and $q < 0.9$ nm^{-1} is described by the power dependence $q - n_3$ with the power factors $n_3 = 3.13 \pm 0.02$ and 2.25 ± 0.02, respectively. Therefore, in the case of Fe_3O_4, scattering takes place on inhomogeneities (aggregates) with a highly developed fractal phase interface with the dimension $D_{S3} = 6 - n_3 = 2.87 \pm 0.02$, while

the power factor for γ-Fe_2O_3/α-Fe_2O_3 corresponds to scattering by objects (aggregates) with mass fractal aggregation of inhomogeneities and fractal dimension $D_{M3} = n_3 = 2.25 \pm 0.02$. The lower limit of self-resemblance for fractal aggregates of a given structural level is determined by the characteristic size R_{c2} of fractal clusters of the second structural level. The absence of deviations of the scattering cross section $d\Sigma(q)/d\Omega$ values from the power law $q - n_3$ at low transferred moments q for both samples indicates that the upper limit of self-similarity of mass fractal aggregates R_{c3} of the third structural level in the both cases significantly exceeds the maximum size that can be determined using the applied technique. Nevertheless, according to the expression $R_{\max} \approx 3.5/q_{\min}$ [40], this size can be estimated on the level $R_{c3} > 70$ nm.

Thus, the observed SAXS pattern for the synthesized iron oxides clearly indicates three types of scattering inhomogeneities significantly differing in their characteristic scale. For a general analysis of the observed scattering, we used an integrated exponential-power equation, taking into account the presence of several structural levels in the scattering system [42]:

$$\frac{d\Sigma(q)}{d\Omega} = \sum_{i=1}^{2}\left[G_i \exp\left(-\frac{q^2R_{gi}^2}{3}\right) + B_i \exp\left(-\frac{q^2R_{g(i-1)}^2}{3}\right)\left(\frac{(\mathrm{erf}(qR_{gi}/\sqrt{6}))^3}{q}\right)^{n_i}\right] + I_{inc}. \quad (3)$$

The summation according to (3) is performed for the number of structural levels. In the most general case, expression (3) determines the presence of four free parameters for each structural level, including the Guinier prefactor G_i, the gyration radius R_{gi}, the power prefactor B_i and the power factor n_i. The parameter I_{inc} is a q-independent constant determined by incoherent scattering.

To obtain the final results according to the equation (3), the experimental dependences of the differential SAXS scattering cross section $d\Sigma(q)/d\Omega$ were processed using the least squares method (LSM) in the entire range under study. The results of this analysis are presented in Fig. 4 and Table 3.

The integrated analysis of SEM data, low-temperature nitrogen adsorption, and SAXS indicates that γ-Fe_2O_3/α-Fe_2O_3 and Fe_3O_4 samples synthesized via the sol-gel technology are porous systems with a three-level hierarchical organization of the structure with different characteristic scales and aggregation types for each of the structural levels, and the characteristic size R_{c3} for the largest third level in both cases exceeds 70 nm. Thus, the first structural level of γ-Fe_2O_3/α-Fe_2O_3 powder consists of almost smooth particles with the characteristic size $R_{c1} \approx 5$ nm, which at the second structural level aggregate into mass fractal clusters with the dimension $D_{M2} = 2.69$ and the upper limit of self-resemblance similarity $R_{c2} \approx 18$ nm, from which mass-fractal aggregates with dimension $D_{M3} = 2.25$ are formed at the third structural level. In turn, the Fe_3O_4 powder at the first structural level also consists of small particles ($R_{c1} \approx 2$ nm) with an almost smooth surface, which at the second structural level aggregate into surface fractal clusters with the dimension of $D_{S2} = 2.58$ and the upper self-resemblance boundary $R_{c2} \approx 6$ nm, from which surface fractal aggregates with the dimension $D_{S3} = 2.87$ are formed at the third structural level.

The magnetization $\boldsymbol{M}$ measured by the induction method for the synthesized Fe_3O_4 and γ-Fe_2O_3/α-Fe_2O_3 powders depending on the applied magnetic field $\boldsymbol{H}$ is shown in Fig. 5. These data indicate almost linear dependences without a hysteresis, suggesting these powders to be soft magnetic materials. However, in the range of applied magnetic fields $\boldsymbol{H}$, the saturation of magnetization $\boldsymbol{M}$ in the studied superparamagnetic nanoparticles was not achieved.

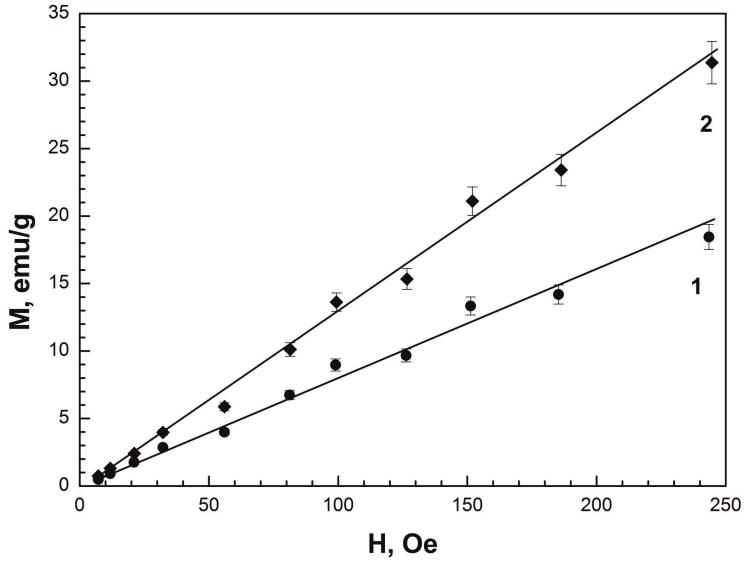

FIG. 5. Magnetization M of Fe_3O_4 (1) and γ-Fe_2O_3/α-Fe_2O_3 (2) as function of the applied magnetic field $\boldsymbol{H}$

The magnetic structure, i.e. spatial distribution and nature of spin correlations in the studied powders of iron oxides, was studied using SAPNS method. Two-dimensional intensities of scattering by iron oxide powders obtained for two polarization states of the neutron beam $I^-(q,\alpha)$ and $I^+(q,\alpha)$ when measured in "zero" ($\boldsymbol{H} \approx 0$) and horizontal magnetic fields ($\boldsymbol{H} = 1T$), respectively, as well as their difference $\Delta I_{MN}(q,\alpha) = I^-(q,\alpha) - I^+(q,\alpha)$ (magnetic-nuclear interference term) during measurements in an external magnetic field. As can be seen from Fig. 6, for the spectra measured in a magnetic field $\boldsymbol{H} = 1T$, the observed scattering pattern is anisotropic with a significant change in the aspect ratios for the two polarization states. The difference signal $\Delta I_{MN}(q,\alpha)$, where all background contributions are self-subtracted, shows an angular dependence on α, with an insignificant intensity along the direction of the applied magnetic field $\boldsymbol{H}$.

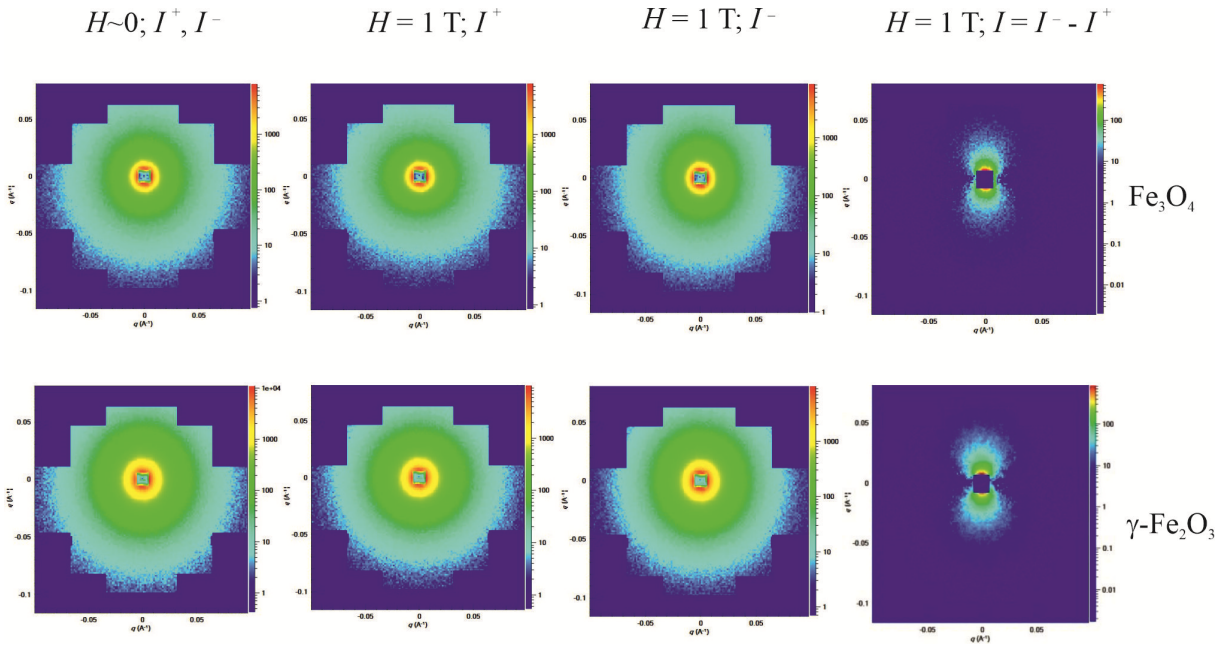

FIG. 6. Experimental two-dimensional intensities of scattering for two polarization states of the incident neutron beam and their difference $\Delta I_{MN}(q,\alpha) = I^-(q,\alpha) - I^+(q,\alpha)$ (magnetic-nuclear interference term) obtained for the synthesized iron oxide powders at measurements in external magnetic field $\boldsymbol{H} = 1T$. The square in the center of the detector is the trace from the beam absorber (beamstop)

The separated nuclear $\langle F_N^2(q)\rangle$, magnetic $\langle F_M^2(q)\rangle_{\mathbf{H}=1T}$ and interference $\langle F_N(q)F_M(q)\rangle_{\mathbf{H}=1T}$ contributions to the scattering are shown in Fig. 7. The comparison of these data indicates that for all the iron oxide samples the nuclear contribution $\langle F_N^2(q)\rangle$ exceeds the magnetic contribution $\langle F_M^2(q)\rangle_{\mathbf{H}=1T}$ by almost an order of magnitude.

3.1.1. Nuclear SAPNS.. The scattering behavior observed for the nuclear component $d\Sigma N(q)/d\Omega$ SANS (Fig. 7) is similar to that revealed for the studied iron oxides using SAXS techniques (Fig. 4) within the used range of transferred momentum $0.08 < q < 1$ nm^{-1}. For γ-Fe_2O_3/α-Fe_2O_3 (Fig. 7(b)), the $d\Sigma N(q)/d\Omega$ plot also features with three q ranges with the nuclear SANS $d\Sigma N(q)/d\Omega$ component following power laws $q^{-\Delta}$ with different power factors $\Delta = n_1, n_2$, and n_3, respectively. In the case of Fe_3O_4 (Fig. 7(a)) only two q regions with different power laws are found for the nuclear component of $d\Sigma N(q)/d\Omega$. This difference is determined by the fact that in the performed experiments $q_{\max} = 1$ nm^{-1}, while in SAXS measurements, scattering from the particles of the first structural level was detected at $q > 1.5$ nm^{-1}. Thus, the analysis of nuclear SANS for the synthesized Fe_3O_4 (Fig. 7(a)) and γ-Fe_2O_3/α-Fe_2O_3 (Fig. 7(b)) samples also involved the integrated exponential-power expression (3) taking into account several structural levels in the scattering system.

To obtain the final results, equation (3) was reduced in couple with the setup resolution function and processed according to the least square method. Thus, obtained data are summarized in Fig. 7 and Table 4.

As shown in Table 4, the atomic supramolecular structure parameters of the synthesized samples based on SANS data are in full agreement with the results obtained from the analysis of SAXS data (Table 3).

3.1.2. SAPNS magnetic scattering $d\Sigma M(q)/d\Omega$ ($\boldsymbol{H} = 1T$). For superparamagnetic nanoparticles, upon saturation of the magnetization, magnetic scattering becomes completely anisotropic, while nuclear scattering remains isotropic. As can be seen from Fig. 7, the magnetic scattering cross section $d\Sigma M(q)/d\Omega$, isolated from the total SAPNS, in the direction $\alpha = \pi/2$, perpendicular to the applied magnetic field $\boldsymbol{H} = 1T$, for iron oxide powders synthesized by the sol-gel technology is small (not more than 10 %) in comparison with nuclear scattering $d\Sigma N(q)/d\Omega$ and is statistically resolvable only in the region of small $q < 0.15$ nm^{-1}, which corresponds to scattering by large-scale magnetic fluctuations appeared to upon the achievement of magnetization saturation.

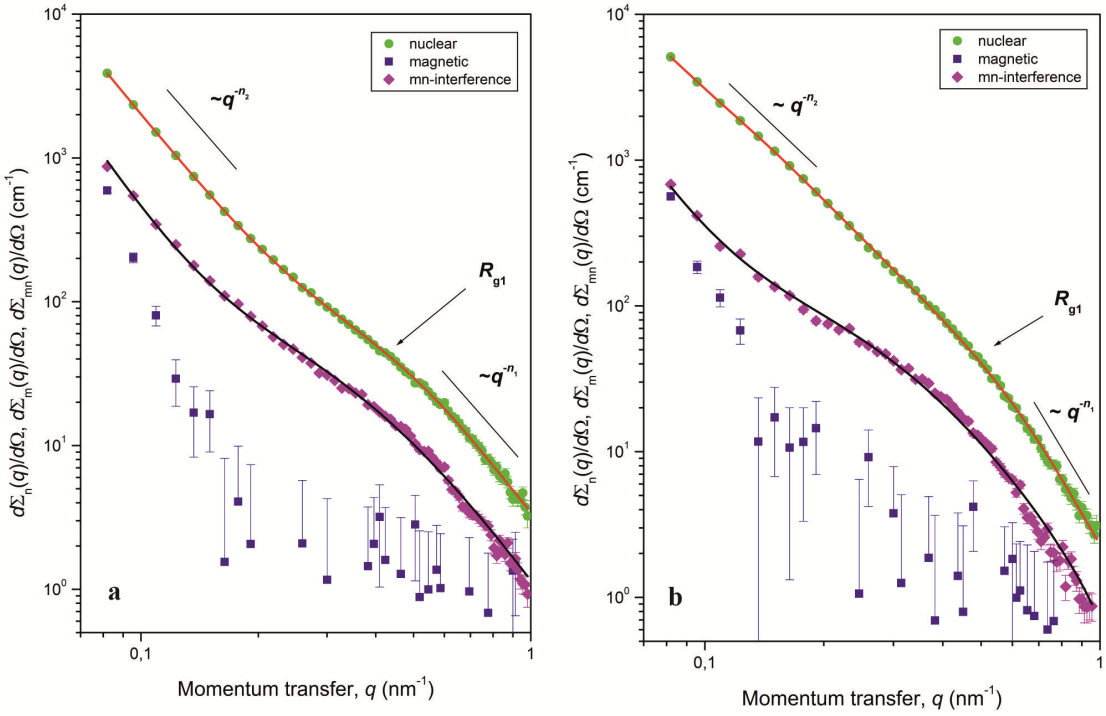

FIG. 7. Nuclear $d\Sigma N(q)/d\Omega$ (◯), magnetic $d\Sigma M(q)/d\Omega$ (□) and magnetic-nuclear interference $d\Sigma_{MN}(q)/d\Omega$ (◊) SAXS cross-dections for Fe_3O_4 (a) and γ-Fe_2O_3/α-Fe_2O_3 (b) samples as function of the transferred momentum q. The data are based on the teo-dimentional spectra (Fig. 6) measured in the magnetic field $\boldsymbol{H} = 1T$. Solid lines correspond to the experimental data fits according to equations (3) and (4)

TABLE 4. Mesostructure parameters of the synthesized iron oxide powders obtained from the analysis of SAPNS cross-section $d\Sigma N(q)/d\Omega$ nuclear component

Parameters	Synthesized iron oxides	
	γ-Fe_2O_3/α-Fe_2O_3	Fe_3O_4
3rd structural level		
R_{c3}, nm	> 45	
$D_{M3} = n_3$	2.35 ± 0.02	—
$D_{S3} = 6 - n_3$	—	2.82 ± 0.02
2nd structural level		
$R_{c2} = [(D_{S2,M2} + 2)/D_{S2,M2}]^{1/2} \cdot R_{g2}$, nm	16 ± 3	5.1 ± 0.5
$D_{M2} = n_2$	2.74 ± 0.04	—
$D_{S2} = 6 - n_2$	—	2.46 ± 0.06
1st structural level		
$R_{c1} = \sqrt{(5/3)} \cdot R_{g1}$, nm	5.9 ± 0.8	—
n_1	4.00 ± 0.05	—

In this regard, the quantitative analysis of the observed magnetic scattering $d\Sigma M(q)/d\Omega$ for the synthesized powders of iron oxides is practically impossible. However, this problem can be addressed by the analysis of the interference contribution $d\Sigma_{MN}(q)/d\Omega$ to the overall SAPNS, that is equal to the magnetic scattering amplitude multiplied by the nuclear scattering amplitude, i.e. corresponding to the first (not to the second, as in the case of measuring the magnetic scattering intensity) power of the magnetic scattering amplitude, that determines an increased sensitivity of this method.

3.1.3. SAPNS magnetic-nuclear cross-section $d\Sigma_{MN}(q)/d\Omega$ ($\boldsymbol{H} = 1T$). The analysis of magnetic-nuclear interference scattering $d\Sigma_{MN}(q)/d\Omega$ contribution into the overall SAPNS obtained in the $\alpha = \pi/2$ direction (orthogonal to the applied magnetic field $\boldsymbol{H} = 1T$) shown in Fig. 7 suggests that the magnetic-nuclear interference scattering $d\Sigma_{MN}(q)/d\Omega$ for both γ-Fe_2O_3/α-Fe_2O_3 and Fe_3O_4 is well fitted by the following equation:

$$\frac{d\Sigma_{MN}(q)}{d\Omega} = \frac{A_2}{q^4} + \frac{A_1}{(q^2 + \kappa_{MN}^2)^2}, \tag{4}$$

where A_1 and A_2 are free parameters, and $\kappa_{MN} = 1/R_{MN}$ is the reverse correlation radius of the magnetic-nuclear contrasting (and, consequently, scattering) region. The first term in the equation (4) ($\sim q^{-4}$) corresponds to the scattering on large-scale spin density fluctuations, and the second term is a squared Lorentzian corresponding to scattering on a spin correlator $\langle S_i, S_j \rangle$ exponentially decreasing with distance r in the coordinate representation:

$$\langle S_i S_j \rangle \propto \exp(-\frac{r}{R_{MN}}). \tag{5}$$

To obtain the final results, the expression (4) was combined with the setup resolution function and processed by the least squares method. The processing results are shown in Fig. 7 and Table 5.

TABLE 5. Correlation radii R_{MN} of the magnetic-nuclear interference scattering for the synthesized iron oxide samples, based on the analysis of the magnetic-nuclear interference component of the SAPNS cross-section $d\Sigma N(q)/d\Omega$

Synthesized iron oxides	R_{MN} (nm)
γ-Fe_2O_3/α-Fe_2O_3	3.2 ± 0.4
Fe_3O_4	2.7 ± 0.3

According to the data in Table 5, the characteristic sizes R_{MN} of the magnetic-nuclear cross-correlations, obtained from the analysis of SAPNS results, are smaller than the characteristic sizes R_c of the nuclear inhomogeneities presented in Tables 3 and 4. However, in this case, the characteristic size R_{MN} corresponds to the average size of magnetic-nuclear cross-correlations, instead of its upper limit, as in the case of the characteristic size R_c of nuclear inhomogeneities in the expressions used in the analysis of $d\Sigma N(q)/d\Omega$.

3.1.4. SANS magnetic cross-section $d\Sigma M(q)/d\Omega$ ($\boldsymbol{H} \approx 0T$). Assuming that the nuclear scattering is isotropic and independent on the applied magnetic field, we determined the magnetic contribution $\left\langle F_M^2(q) \right\rangle_{\mathbf{H} \approx 0}$ into the overall SANS intensity in the case of "zero" field ($\boldsymbol{H} \approx 0T$). The corresponding cross-sections $d\Sigma M(q)/d\Omega$ of the magnetic scattering for the studied samples are shown in Fig. 8.

According to Fig. 8, a statistically resolvable magnetic scattering $d\Sigma M(q)/d\Omega$ is observed for γ-Fe_2O_3/α-Fe_2O_3, while in the case of the synthesized Fe_3O_4, a quantitative analysis is almost impossible. However, the presence of a blurry peak with $q_{\max} \approx 0.4$ nm^{-1} at the $d\Sigma M(q)/d\Omega$ plot for this sample (Fig. 8(a)) suggests the presence of magnetic inhomogeneities structured according to a short-range order with the radius of interparticle magnetic correlations $\xi_M = 2\pi/q_{\max} \approx 16$ nm. The magnetic scattering at small q values ($q < 0.2$ nm^{-1}) is probably determined by scattering on large-scale magnetic fluctuations.

A similar blurred peak with $q_{\max} \approx 0.25$ nm^{-1} is observed at $d\Sigma M(q)/d\Omega$ plot for the synthesized γ-Fe_2O_3/α-Fe_2O_3. The magnetic scattering of this samples was analyzed using the expression:

$$\frac{d\Sigma_{M(q)}}{d\Omega} = \frac{A_2}{q^4} + \frac{A_1}{\left((q - q_{\max})^2 + \kappa_M^2\right)^2}, \tag{6}$$

where A_1 and A_2 are free parameters, and $\kappa_M = 1/R_M$ is the reverse correlation radius of magnetic inhomogeneities. The second term in equation (6) corresponds to the scattering on magnetic inhomogeneities structured according to a short-range order with the radius of interparticle magnetic correlations $\xi_M = 2\pi/q_{\max} \approx 25$ nm.

To obtain the final results, expression (6) was combined with the setup resolution function and processed by the least squares method. The processing results are shown in Fig. 8 and Table 6.

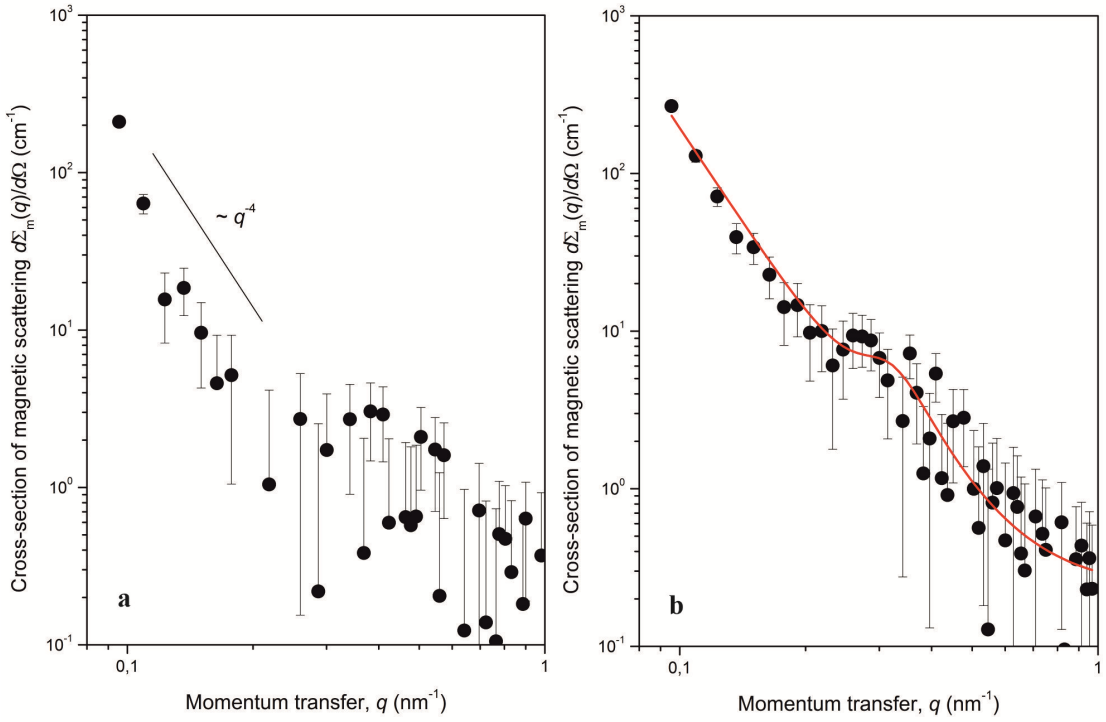

FIG. 8. SANS magnetic cross-sections $d\Sigma M(q)/d\Omega$ in the "zero" field ($\boldsymbol{H} \approx 0$) for the synthesized iron oxides Fe_3O_4 (a) and γ-Fe_2O_3/α-Fe_2O_3 (b) as function of the transferred momentum q. The solid line corresponds to the experimental data fit according to the equation (6)

TABLE 6. Correlation radii R_M of magnetic scattering and interparticle magnetic correlations ξ_M of the synthesized iron oxides, based on the analysis of SANS $d\Sigma M(q)/d\Omega$ cross-section in the "zero" field ($\boldsymbol{H} \approx 0T$)

Synthesized iron oxides	$\xi_M = 2\pi/q_{\max}$ (nm)	R_M (nm)
γ-Fe_2O_3/α-Fe_2O_3	25	4.1 ± 0.9
Fe_3O_4	16	—

3.2. Study of bioactive performances of the synthesized powders

The obtained data concerning to the effect of presowing treatment of spring barley seeds with aqueous suspensions of the synthesized Fe_3O_4 and γ-Fe_2O_3/α-Fe_2O_3 powders on germination performances and biometric indicators of sprout growth are summarized in Table 7. These data show that the treatment of seeds with suspensions of γ-Fe_2O_3/α-Fe_2O_3 or Fe_3O_4 in the previously selected concentrations of 0.01 and 0.001 mg/L does not have a significant effect on their germination and root length of seedlings compared with the control samples. However, the length of seedling sprouts tends to increase or significantly change in values after seed treatment with suspensions of γ-Fe_2O_3/α-Fe_2O_3 in the concentration 0.001 mg/L or Fe_3O_4 in the concentrations of 0.001 and 0.01 mg/L, with the most pronounced effect observed in the case of using a 0.001 mg/L suspension of Fe_3O_4. A slight trend should be also noted towards a decrease in the height of sprouts after seed treatment with suspensions of the tested substances at a higher concentration of 0.01 mg/L.

The revealed tendency to stimulate the growth of spring barley plants at the early stages of development after the treatment of their seeds with aqueous suspensions of the tested substances persisted throughout the ontogeny of plants and, ultimately, resulted in a significant increase in the productivity indicator – the number of productive stems on the plant under favorable growing conditions (Table 8). Noteworthy, the considered effect of seed treatment with aqueous suspensions of iron oxides was not observed in respect of the grain productivity of spring barley, since the values of grain productivity indicators, including the number of seeds and their weight on the plant do not differ significantly from those in the control seeds. Moreover, there is a pronounced trend towards a significant decrease in these indicators of barley grain productivity relative to the control in the case of seed treatment with aqueous suspensions of Fe_3O_4.

The study of the effect of seed treatment on the resistance of plants to the stress factors indicated in Table 8 in the most vulnerable periods of the plants development revealed differences effectiveness of the tested iron oxide additives under different stress conditions.

TABLE 7. Effect of barley seeds (Leningradsky variety) treatment with iron oxide suspensions upon the germination performances and biometric indicators of seedlings growth

Seeds treatment variants	Germination energy		Germination, %		Sprout length		Root length	
	%	% of the reference samples	%	% of the reference samples	cm	% of the reference samples	%	% of the reference samples
Control (treatment with distilled water)	96	100	98	100	8.7±0.6	100	8.6±0.5	100
0.01 mg/l γ-Fe_2O_3/α-Fe_2O_3	88	92	96	98	8.8±0.7	101	8.2±0.5	95
0.001 mg/l γ-Fe_2O_3/α-Fe_2O_3	93	97	95	97	9.3±0.6	107	7.9±0.4	92
0.01 mg/l Fe_3O_4	93	97	97	99	9.2±0.6	106	8.3±0.4	97
0.001 mg/l Fe_3O_4	92	96	95	97	10.1±0.6*	116*	8.6±0.4	100

Note: * the value significantly differs from the control at the 5 % significance level

TABLE 8. Effect of barley seeds (Leningradsky variety) treatment with iron oxide suspensions upon the plants productivity at growing under controlled favorable conditions, after the effect of with UV-B radiation (dose 20.0 kJ/m^2) and soil moisture deficiency (25 – 30 % of the total moisture capacity)

Seeds treatment variants	Number of productive stems, pieces / % of the control	Number of seeds from one plant, pieces / % of the control	Weight of the seeds from one plant, g / % of the control
No stress			
Control (treatment with distilled water)	3.1±0.3 / 100	70.0±5.2 / 100	2.52±0.22 / 100
0.01 mg/l γ-Fe_2O_3/α-Fe_2O_3	4.7±0.6 / 152*	72.0±5.6 / 103	2.60±0.20 / 103
0.01 mg/l Fe_3O_4	3.6±0.4 / 116	60.0±4.2 / 86*	2.22±0.19 / 88
UV-B radiation			
Control (treatment with distilled water)	4.7±0.6 / 152*	58.0±4.8 / 83*	2.10±0.18 / 83*
0.01 mg/l γ-Fe_2O_3/α-Fe_2O_3	4.9±0.7 / 158*	64.3±5.2 / 92	2.36±0.16 / 94
0.01 mg/l Fe_3O_4	3.9±0.5 / 126*	54.0±4.3 / 77*	2.00±0.17 / 79*
Soil moisture deficiency			
Control (treatment with distilled water)	2.2±0.5 / 71*	40.0±3.9 / 57*	1.40±0.14 / 56*
0.01 mg/l γ-Fe_2O_3/α-Fe_2O_3	1.0±0.2 / 32*	44.0±4.2 / 63*	1.60±0.15 / 63*
0.01 mg/l Fe_3O_4	2.7±0.6 / -87	50.0±4.9 / 71*	1.90±0.16 / 75*

Note: * the value significantly differs from the control not stress at the 5 % significance level

Thus, when irradiated with high-intensity UV-B radiation, a significant positive effect on plant productivity is observed in case of seeds treatment with aqueous suspensions of γ-Fe_2O_3/α-Fe_2O_3, providing the target plant performances on the same level or exceeding those for the control samples unaffected by the stress, whereas the control stressed plants, and especially plants treated with an aqueous suspension of Fe_3O_4, reduced the grain productivity by 17 and 21 – 23 %, respectively (Table 8). Under conditions of soil moisture deficiency, seed treatment with tested iron oxide additives showed a positive effect, with a trend to a significantly increased grain productivity of plants relative to stressed reference seeds. Generally, the seed treatment with Fe_3O_4 aqueous suspensions turned out to be more effective in increasing plant resistance to the stressors compared to the treatment with γ-Fe_2O_3/α-Fe_2O_3, apparently due to the formation of a larger number of productive stems and seeds (by 270 and 14 %, respectively).

Thus, aqueous suspensions of the synthesized iron oxides in the concentrations of 0.001 and 0.01 mg/L demonstrate a pronounced biological activity at presowing treatment of spring barley, in respect of stimulating the plants growth at the early stages of their development and increasing the number of productive stems under favorable conditions for the vital activity of plants. However, during the cultivation of spring barley under stressful conditions in the most vulnerable periods of plant development, significant differences were revealed in the effectiveness of the influence of the tested iron oxide additives on the plant resistance, depending on the acting stressor. The treatment of seeds with a suspension of γ-Fe_2O_3/α-Fe_2O_3 in the concentration of 0.01 mg/L provided an effective protection from a negative impact of high-intensity UV-B radiation upon the plant productivity remaining on the same level as for the reference plants tested under favorable conditions. In respect of protection from soil moisture deficiency, treatment with 0.01 mg/L Fe_3O_4 suspension was found to be more effective against the reduction of the productivity indicators.

4. Conclusion

Powdered iron oxides prepared via sol-gel method are studied using a number of characterization techniques, including XRD, SEM, low temperature nitrogen adsorption, small angle X-ray (SAXS) and polarized neutron scattering (SAPNS). The synthesized γ-Fe_2O_3/α-Fe_2O_3 and Fe_3O_4 samples are defined as porous systems with a three-level hierarchical structural organization featuring with different characteristic scales and aggregation types for each of the structural levels. The characteristic size R_{c3} for the largest scale third level in both cases exceeds 70 nm. In γ-Fe_2O_3/α-Fe_2O_3 powder, the first structural level consists of almost smooth particles with the characteristic size $R_{c1} \approx 5$ nm, aggregating at the second structural level into mass fractal clusters with the dimension $D_{M2} = 2.69$ and the upper limit of self-resemblance $R_{c2} \approx 18$ nm, in turn, forming mass fractal aggregates with the dimension $D_{M3} = 2.25$ at the third structural level. In Fe_3O_4 powder, the first structural level also consists of small particles ($R_{c1} \approx 2$ nm) with an almost smooth surface, aggregating at the second structural level into surface-fractal clusters with a dimension of $D_{S2} = 2.58$ and an upper self-resemblance boundary $R_{c2} \approx 6$ nm, forming surface fractal aggregates with the dimension $D_{S3} = 2.87$ at the third structural level.

A detailed analysis of the SAPNS data revealed that the magnetic structure of Fe_3O_4 and γ-Fe_2O_3/α-Fe_2O_3 powders synthesized via sol-gel process consists of superparamagnetic particles with a characteristic radius of magnetic-nuclear cross-correlations $R_{MN} \approx 3$ nm. Moreover, short-range spin correlations are also observed between these superparamagnetic particles with the interparticle magnetic correlation radii $\xi_M \approx 16$ and 25 nm for Fe_3O_4 and γ-Fe_2O_3/α-Fe_2O_3, respectively.

A relationship is revealed between the crystallographic modification and biological activity of the synthesized iron oxide powders towards the seeds of spring barley of the Leningradsky variety. Although the presowing treatment of seeds with Fe_3O_4 and γ-Fe_2O_3/α-Fe_2O_3 suspensions does not affect their germination and the length of roots and sprouts, it stimulates the other plants growth indicators and affects the plants productivity in different ways depending on their growing conditions. Particularly, γ-Fe_2O_3/α-Fe_2O_3 suspension demonstrated a higher efficiency in respect of the productivity and resistance of spring barley plants under favorable conditions and under stressful exposure to UV-B radiation, while the suspension of Fe_3O_4 is more effective under stressful conditions in terms of moisture content in the soil.

References

[1] Samrot A.V., Sahithya C. Sai, et al. A review on synthesis, characterization and potential biological applications of superparamagnetic iron oxide nanoparticles. *Current Research in Green and Sustainable Chemistry*, 2021, **4**, 100042.

[2] Song C., Sun W., Xiao Yu., Shi X. Ultrasmall iron oxide nanoparticles: synthesis, surface modification, assembly, and biomedical applications. *Drug Discovery Today*, 2019, **24** (3), P. 835–844.

[3] Bhateria R., Singh R. A review on nanotechnological application of magnetic iron oxides for heavy metal removal. *J. of Water Process Engineering*, 2019, **31**, 100845.

[4] Sheikholeslami Z., Yousefi Kebria D., Qaderi F. Application of γ-Fe_2O_3 nanoparticles for pollution removal from water with visible light. *J. of Molecular Liquids*, 2020, **299**, 112118.

[5] Wang W., Li F., et al. M2 macrophage-targeted iron oxide nanoparticles for magnetic resonance image-guided magnetic hyperthermia therapy. *J. of Materials Science & Technology*, 2021, **81**, P. 77–87.

[6] Li M., Zhang P., et al. Physiological impacts of zero valent iron, Fe_3O_4 and Fe_2O_3 nanoparticles in rice plants and their potential as Fe fertilizers. *Environmental Pollution*, 2021, **269**, 116134.

[7] Pariona N., Martínez A.I., Hernandez-Flores H., Clark-Tapia R. Effect of magnetite nanoparticles on the germination and early growth of Quercus macdougallii. *Science of The Total Environment*, 2017, **575**, P. 869–875.

[8] Li J., Hu J., et al. Uptake, translocation and physiological effects of magnetic iron oxide (γ-Fe_2O_3) nanoparticles in corn (Zea mays L.). *Chemosphere*, 2016, **159**, P. 326–334.
[9] Iannone M.F., Groppa M.D., et al. Impact of magnetite iron oxide nanoparticles on wheat (Triticum aestivum L.) development: Evaluation of oxidative damage. *Environmental and Experimental Botany*, 2016, **131**, P. 77–88.
[10] Tombuloglu H., Slimani Y., et al. Uptake and translocation of magnetite (Fe_3O_4) nanoparticles and its impact on photosynthetic genes in barley (Hordeum vulgare L.). *Chemosphere*, 2019, **226**, P. 110–122.
[11] Yan L., Li P., et al. Physiological and metabolic responses of maize (Zea mays) plants to Fe_3O_4 nanoparticles. *Science of the Total Environment*, 2020, **718**, 137400.
[12] Ding Y., Bai X., et al. Toxicological responses of Fe_3O_4 nanoparticles on Eichhornia crassipes and associated plant transportation. *Science of the Total Environment*, 2019, **671**, P. 558–567.
[13] Wang Y., Wang S., et al. The impacts of γ-Fe_2O_3 and Fe_3O_4 nanoparticles on the physiology and fruit quality of muskmelon (Cucumis melo) plants. *Environmental Pollution*, 2019, **249**, P. 1011–1018.
[14] Cai L., Jia H., et al. Foliar exposure of Fe_3O_4 nanoparticles on Nicotiana benthamiana: Evidence for nanoparticles uptake, plant growth promoter and defense response elicitor against plant virus. *J. of Hazardous Materials*, 2020, **393**, 122415.
[15] Konate A., Wang Y., et al. Comparative effects of nano and bulk-Fe_3O_4 on the growth of cucumber (Cucumis sativus). *Ecotoxicology and Environmental Safety*, 2018, **165**, P. 547–554.
[16] Nisticò R. A synthetic guide toward the tailored production of magnetic iron oxide nanoparticles. *Boletín de la Sociedad Española de Cerámica y Vidrio*, 2021, **60** (1), P. 29–40.
[17] Lastovina T.A., Budnyk A.P., Kubrin S.P., Soldatov A.V. Microwave-assisted synthesis of ultra-small iron oxide nanoparticles for biomedicine. *Mendeleev Communications*, 2018, **28** (2), P. 167–169.
[18] Calderón P.A., Pablo B., et al. Magnetic iron oxides nanoparticles obtained by mechanochemical reactions from different solid precursors. *J. of Alloys and Compounds*, 2021, **860**, 157892.
[19] Bhavani P., Rajababu C.H., et al. Synthesis of high saturation magnetic iron oxide nanomaterials via low temperature hydrothermal method. *J. of Magnetism and Magnetic Materials*, 2017, **426**, P. 459–466.
[20] Jafari Eskandari M., Hasanzadeh I. Size-controlled synthesis of Fe_3O_4 magnetic nanoparticles via an alternating magnetic field and ultrasonic-assisted chemical co-precipitation. *Materials Science and Engineering: B*, 2021, **266**, 115050.
[21] Koizumi H., Azhar Uddin Md, Kato Y. Effect of ultrasonic irradiation on γ-Fe_2O_3 formation by co-precipitation method with Fe^{3+} salt and alkaline solution. *Inorganic Chemistry Communications*, 2021, **124**, 108400.
[22] Xu J., Yang H., et al. Preparation and magnetic properties of magnetite nanoparticles by sol-gel method. *J. of Magnetism and Magnetic Materials*, 2007, **309** (2), P. 307–311.
[23] Hasanpour A., Niyaifar M., Asan M., Amighian J. Synthesis and characterization of Fe_3O_4 and ZnO nanocomposites by the sol-gel method. *J. of Magnetism and Magnetic Materials*, 2013, **334**, P. 41–44.
[24] Okorokov A.I., Grigor'ev S.V., et al. New magnetic phenomena and polarized neutrons. *Surf. Investigation. X-ray, Synchrotron Neutron Techniq*, 2007, **1**, P. 542–555.
[25] Muhlbauer S., Honecker D., et al. Magnetic small-angle neutron scattering. *Reviews of Modern Physics*, 2019, **91**, 015004.
[26] Runov V., Glattli H., et al. Small-angle polarized neutron scattering in $Sm_{1-x}Sr_xMnO_3$ ($x < 0.5$) perovskite. *Physica B*, 2000, **276–278**, P. 795–796.
[27] Bergenti I., Deriu A., et al. Small angle polarised neutron scattering investigation of magnetic nanoparticles. *J. of Magnetism and Magnetic Materials*, 2003, **262** (1), P. 60–63.
[28] Runov V.V., Bugrov A.N., et al. Mesostructure of Composite Materials Based on Segmented Poly(Urethane Imide) Containing Ferrite Nanoparticles. *Rus. J. of Inorganic Chemistry*, 2021, **66**, P. 225–236.
[29] Runov V.V., Bugrov A.N., et al. Magnetic Neutron Scattering in Reduced Graphene Oxide. *JETP Letters*, 2021, **113**, P. 384–388.
[30] Shilova O., Panova G., et al. Aqueous Chemical Co-Precipitation of Iron Oxide Magnetic Nanoparticles for Use in Agricultural Technologies. *Letters in Applied NanoBioScience*, 2021, **10** (2), P. 2215–2239.
[31] Wignall G.T., Bates F.S. Absolute calibration of small-angle neutron scattering data. *J. Appl. Crystallogr.*, 1987, **20**, P. 28–40.
[32] Jülich Centre for Neutron Science, QtiKWS 2019, URL: www.qtisas.com.
[33] Panova G.G., Chernousov I.N., et al. Scientific basis for large year-round yields of high-quality crop products under artificial lighting. *Russian Agricultural Sciences*, 2015, **41**, P. 335–339.
[34] Beaucage G., Ulibarri T.A., Black E.P., Schaefer D.W. In Mark J., et al. (eds) *Multiple Size Scale Structures in Silica–Siloxane Composites Studied by Small-Angle Scattering*. American Chemical Society, Washington, 1995.
[35] Štěpánek M., Matějíček P, et al. Polyelectrolyte–Surfactant Complexes Formed by Poly[3,5-bis(trimethylammoniummethyl)4-hydroxystyrene iodide]-block-poly(ethylene oxide) and Sodium Dodecyl Sulfate in Aqueous Solutions. *Langmuir*, 2011, **27** (9), P. 5275–5281.
[36] Khamova T.V., Kopitsa G.P., et al. The Structure and Properties of TiO_2 Nanopowders_for Use in Agricultural Technologies. *Biointerface Research in Applied Chemistry*, 2021, 11 (4), P. 12285–12300.
[37] Guinier A., Fournet G. *Small-angle scattering of X-rays*. John Wiley and Sons, Inc, New York, 1955.
[38] Oh C., Sorensen C.M. The Effect of Overlap between Monomers on the Determination of Fractal Cluster Morphology. *J. Colloid Interface Sci.*, 1997, **193** (1), P. 17–25.
[39] Porod G. Die Röntgenkleinwinkelstreuung von dichtgepackten kolloiden Systemen. *Kolloid-Zeitschrift*, 1952, **125**, P. 51–57.
[40] Bale H.D., Schmidt P.W. Small-Angle X-Ray-Scattering Investigation of Submicroscopic Porosity with Fractal Properties. *Phys. Rev. Lett.*, 1984, **53**, 596.
[41] Teixeira J. In: Stanley HE, Ostrowsky N. (eds) Experimental methods for studying fractal aggregates. Springer, Dordrecht, 1986.
[42] Beaucage G. Approximations Leading to a Unified Exponential / Power-Law Approach to Small-Angle Scattering. *J. Appl. Crystallogr.*, 1995, **28**, P. 717–728.

Submitted 18 May 2022; revised 20 May 2022; accepted 30 July 2022

Information about the authors:

Tamara V. Khamova – Institute of Silicate Chemistry of Russian Academy of Sciences, emb. Makarova, 2, St. Petersburg, 199034, Russia; ORCID 0000-0003-4302-3520; tamarakhamova@gmail.com

Olga A. Shilova – Institute of Silicate Chemistry of Russian Academy of Sciences, emb. Makarova, 2, St. Petersburg, 199034, Russia; ORCID 0000-0002-3856-9054; olgashilova@bk.ru

Yulia E. Gorshkova – Joint Institute for Nuclear Research, St. Joliot-Curie, 6, Dubna, Moscow Region, 141980, Russia; ORCID 0000-0002-5016-1553; Yulia.Gorshkova@jinr.ru

Natalia V. Tsvigun – Institute of Crystallography Federal R&D Center "Crystallography and Photonics" of the Russian Academy of Sciences, Leninsky pr., 59, Moscow, 119333, Russia; ORCID 0000-0003-2028-8067; n_tsvigun@mail.ru

Oleg V. Gerashchenko – Petersburg Nuclear Physics Institute named by B. P. Konstantinov of National Research Centre Kurchatov Institute, Orlova roshcha, 1, Gatchina, Leningrad Region, 188300, Russia; ORCID 0000-0003-1951-4805; gerashchenko_ov@pnpi.nrcki.ru

Alexander E. Baranchikov – Kurnakov Institute of General and Inorganic Chemistry of the Russian Academy of Sciences, Leninsky pr., 31, Moscow, 119991, Russia; ORCID 0000-0002-2378-7446; a.baranchikov@yandex.ru

Olga R. Udalova – Agrophysical Research Institute, Grazhdansky pr., 14, St. Petersburg, 195220, Russia; ORCID 0000-0003-3521-0254; udal59@inbox.ru

Anna S. Zhuravleva – Agrophysical Research Institute, Grazhdansky pr., 14, St. Petersburg, 195220, Russia; ORCID 0000-0002-6367-0728; zhuravlan@gmail.com

Gaiane G. Panova – Agrophysical Research Institute, Grazhdansky pr., 14, St. Petersburg, 195220, Russia; ORCID 0000-0002-1132-9915; gaiane@inbox.ru

Gennady P. Kopitsa – Institute of Silicate Chemistry of Russian Academy of Sciences, emb. Makarova, 2, St. Petersburg, 199034, Russia; Petersburg Nuclear Physics Institute named by B. P. Konstantinov of National Research Centre Kurchatov Institute, Orlova roshcha, 1, Gatchina, Leningrad Region, 188300, Russia; ORCID 0000-0002-0525-2480; kopitsa_gp@pnpi.nrcki.ru

Conflict of interest: the authors declare no conflict of interest.